

# 2024 S.T. Yau High School Science Award

## Investigation of Rotational Dynamics in Asymmetric Acoustic Fields Within Acoustic Levitation Systems

### The Team

Name of team member: YUAN ZIOU  
School: Shenzhen College of International Education  
Country: CHINA

Name of team member: YANG RUI  
School: Shenzhen College of International Education  
Country: CHINA

Name of supervising teacher: YANG YIMING  
Job Title: Physics Teacher  
School: The High School Attached To Hunan Normal  
University  
Country: CHINA

# Abstract

Our investigation began with a childhood fascination with a swimming pool, where swiftly rotating our hands created vortices that effortlessly spun bubbles within swirling currents. This led us to wonder if this mesmerizing rotational phenomenon could also occur in air—a lighter, more universal medium. Just as our hands manipulated water, we found that acoustic levitation could harness standing waves to manipulate air. During experiments, we unexpectedly observed the rotational motion of levitated objects under specific parameters.

This paper delves into the root cause of this rotation, focusing on key factors that drive the angular velocity of objects in asymmetric acoustic fields. Through a novel experimental setup, we explored the existing torques at play, offering deeper insights into the rotational dynamics of levitated particles. Our findings aim to bridge the research gap in acoustic levitation studies and have potential applications in areas where non-contact, precise manipulation is critical, such as material science and biotechnology.

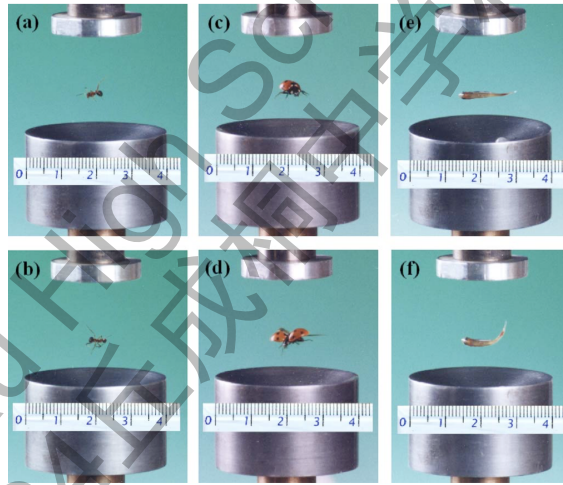


Figure 1: an interesting example of acoustic levitation: levitating insects[19]

# Contents

<b>1</b>	<b>Motivation and Introduction</b>	<b>4</b>
<b>2</b>	<b>Experimental Setup and Numerical Simulation Model</b>	<b>6</b>
2.1	Experimental Setup . . . . .	6
2.1.1	Generation of Ultrasound and Monitoring of Electrical Signals	6
2.1.2	Support Configuration, Reflector Fixture, and Three-Dimensional Platform . . . . .	7
2.1.3	Kinematic Vision Tracking System . . . . .	8
2.2	Tracker Configuration . . . . .	9
2.3	Simulation Configuration . . . . .	11
2.4	MATLAB Approximation Model . . . . .	11
2.5	COMSOL Modelling and Regularity Discussion . . . . .	15
<b>3</b>	<b>Experimental Data and Numerical Simulation Results Analysis</b>	<b>18</b>
3.1	Validation of MATLAB Simulation . . . . .	18
3.2	Relationship between Applied Voltage and the Angular Velocity of Polystyrene Spheres (with fixed X-offset) . . . . .	20
3.3	Relationship between the X-offset of the Reflector and the Rotating Sphere's Angular Velocity . . . . .	24
<b>4</b>	<b>Discussion</b>	<b>27</b>
4.1	Theory Discussion . . . . .	27
4.1.1	Toques Acting on the Rotating Sphere . . . . .	28
4.1.2	Discussion on the Existence of Torque . . . . .	29
4.1.3	Factors Affecting Angular Velocity . . . . .	31
4.1.4	The Effect of Gravity on the Equilibrium Axial Displacement of the Centre of the Spherical Sample . . . . .	32
4.2	Limitations . . . . .	33
4.2.1	Measurements . . . . .	33
4.2.2	Experimental Environment . . . . .	34
<b>5</b>	<b>Summary</b>	<b>35</b>
5.1	Conclusion . . . . .	35
5.2	Future Work . . . . .	36
<b>A</b>	<b>Acknowledgements</b>	<b>39</b>
<b>B</b>	<b>MATLAB Source Code</b>	<b>40</b>

# 1 Motivation and Introduction

Spin angular momentum is a universal feature, widely observed in natural systems [11] including spin angular momentum in electromagnetic fields and even in quantum fields. Recently, researchers have demonstrated that spin angular momentum can be carried by longitudinal sound wave[17], manifesting as a circulation of the fluid velocity field. In acoustics, spin angular momentum often describes the rotation of a local particle velocity vector field. [12] This phenomenon has opened new avenues for wave-matter interactions, such as the manipulation of levitated objects, and has great potential applications in areas like drop dynamics, high-temperature material processing, and bioreactors, particularly due to the zero-contact nature of acoustic levitation [5][18][14].

It is important to distinguish spin angular momentum from orbital angular momentum, which is commonly observed in acoustic vortices. Acoustic vortices generate helicoidal wavefronts with null-pressure centers, creating structured paths for manipulating levitated objects using large arrays of transducers[3]. Recent advances include the work of Junfei Li et al, who developed three-dimensional acoustic tweezers using vortex streaming[9], and Z.Y. Hong et al, who explored potential-well structures in acoustic vortex fields[5]. These studies rely on multiple transducers generating vortex fields through phase-shifted sinusoidal signals. In contrast, spin angular momentum is derived from the rotation of the polarization[17], as described by the particle velocity field vector, and has only recently begun to receive focused study.[16]

Despite the extensive research on orbital angular momentum in acoustic vortices, the spinning behavior caused by acoustic spin angular momentum remains under-explored. While previous studies have primarily focused on generating rotational motion in the air using complex, multi-transducer setups, little has been done to explore simpler methods of generating spin angular momentum.

In this study, we proposed a novel method for inducing spin angular momentum in an asymmetric acoustic field using a single piezoelectric transducer and a curved reflector. The curved reflector enhanced the acoustic field's strength and created an asymmetry that induced rotational motion in levitated polystyrene spheres[20]. How factors such as the X-offset between the transducer and reflector, the distance between the two, and the spinning behavior of the spheres were investigated.

The relationship between input voltage and the angular velocity of the spheres was discussed. Our experimental results demonstrated a strong linear correlation between these variables, indicating that angular velocity is proportional to the input

voltage. To verify these findings, MATLAB and COMSOL simulations to model the acoustic pressure and velocity fields were employed. The simulations showed strong agreement with the experimental data, providing a comprehensive understanding of the system's dynamics.

2024 S.-T. Yau High School Science Award  
仅用于2024丘成桐中学科学奖论文公示

## 2 Experimental Setup and Numerical Simulation Model

This section outlines the experimental setup and the numerical simulations used to investigate the rotational dynamics of levitated spheres in an asymmetric acoustic field. The section is divided into multiple stages, including the generation of ultrasound, monitoring electrical signals, kinematic tracking, and simulation techniques using MATLAB and COMSOL.

### 2.1 Experimental Setup

#### 2.1.1 Generation of Ultrasound and Monitoring of Electrical Signals

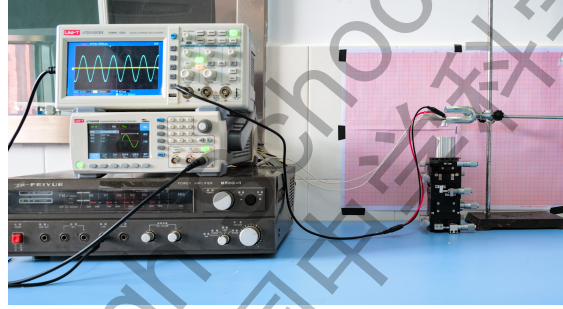


Figure 2: Experimental Setup

The experimental setup, as shown in Figure 2, can be broken down into three key components: the ultrasound generation and signal monitoring system, the support and reflector configuration, and the kinematic vision tracking system. These components work in tandem to create and observe the acoustic field that governs the behavior of the levitated spheres.

To generate the ultrasound required for the levitation, a 40 kHz ultrasonic transducer was used (as shown in Figure 3). The transducer requires high-power input, so we employed a waveform generator and a power amplifier, connected in a configuration that is illustrated in Figure 5.

The system's waveform generator (UNI-T UTG6005B) outputs a sinusoidal wave, while a dual-channel oscilloscope (UNI-T UTD2102CEX 100MHz) is used for monitoring the waveforms. Channel 1 (CH1) monitors the waveform generated by the waveform generator, and Channel 2 (CH2) captures the output waveform

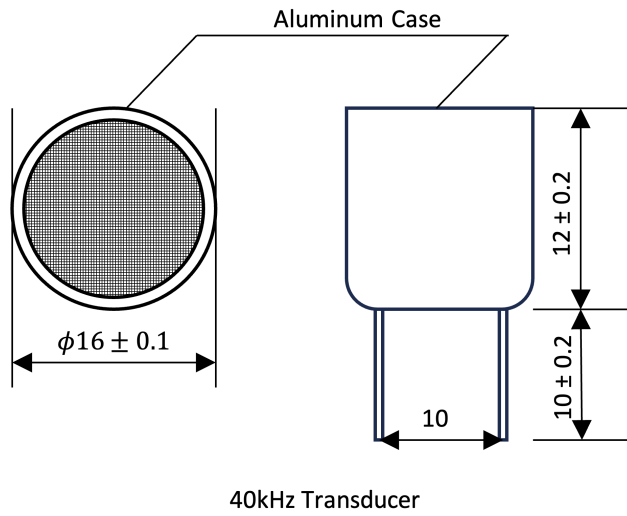


Figure 3: 40kHz Transducer Geometry Diagram



Figure 4: Physical Transducer Example

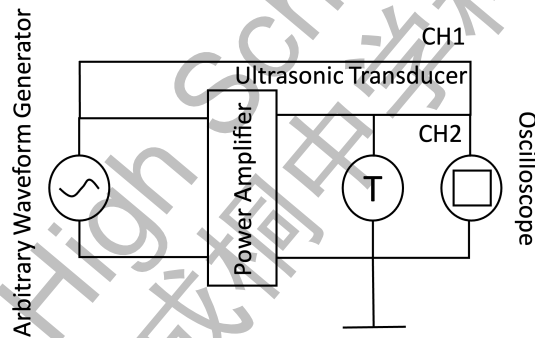


Figure 2.3

Figure 5: Experimental Setup Circuit Diagram

from the power amplifier, which is equivalent to the transducer's signal. Figures 6 and 7 show example waveforms captured during the experiment.

### 2.1.2 Support Configuration, Reflector Fixture, and Three-Dimensional Platform

The main levitation experiments were conducted in a 3-D space between the transducer and a reflector. The reflector fixture was mounted on a three-dimensional platform, allowing precise displacement in the x, y, and z directions. These displacements were measured using a vernier scale on the 3-D platform with a division

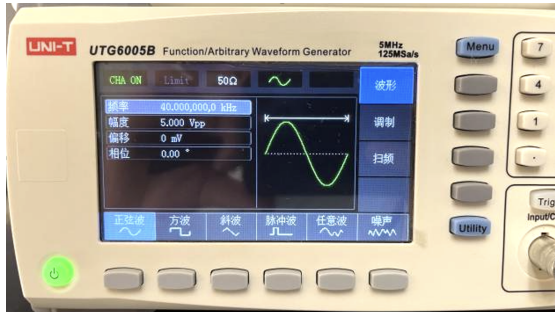


Figure 6: Waveform Generator Reading  
Frequency = 40kHz

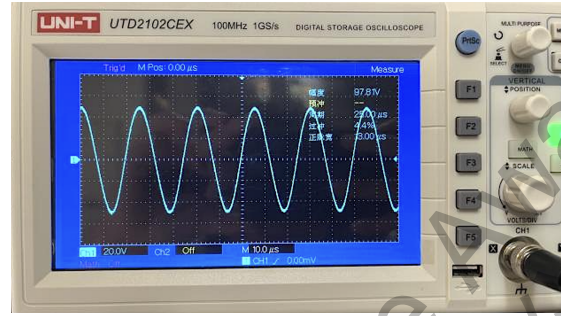


Figure 7: Oscilloscope Reading Voltage  
Input = 97.81V

scale of 0.01mm (shown in Figure 10)

The reflector used in the experiments was a cylindrical aluminum structure (Figure 8) with a 40 mm diameter, a 40 mm height, and a curvature radius of 28 mm. Figure 9 illustrates the geometric parameters of the reflector's curved surface[20]. The ultrasonic transducer was fixed above the reflector, and the setup was secured by drilling two holes (10 mm apart) in a square acrylic board using a laser cutter. The transducer was mounted on the board and connected to both the power amplifier and the waveform generator. The entire structure was stabilized using a clamp on an iron frame stand. A spirit level ensured that the transducer's plane remained horizontal.

### 2.1.3 Kinematic Vision Tracking System

To record the rotational dynamics of levitated spheres, we employed a high-speed camera (Nikon Z8) capable of capturing high-quality video at 120 frames per second. The camera was mounted on a tripod with three-axis locks to ensure stability during recording. The camera's built-in digital level helped ensure both horizontal and vertical alignment. To minimize parallax error, we adjusted the tripod height and monitored the camera's screen until the reflector and transducer were precisely aligned along a horizontal axis.

For capturing the high-speed rotation of the spheres, the camera was set to a shutter speed of 1/4000s, with an aperture of f/9 and an ISO of 4000. To ensure sufficient lighting, two lamps were used—one positioned to illuminate the y-plane and another placed behind the levitation system to light up the x-plane (shown in Figure 12)



Figure 8: Aluminium Reflector

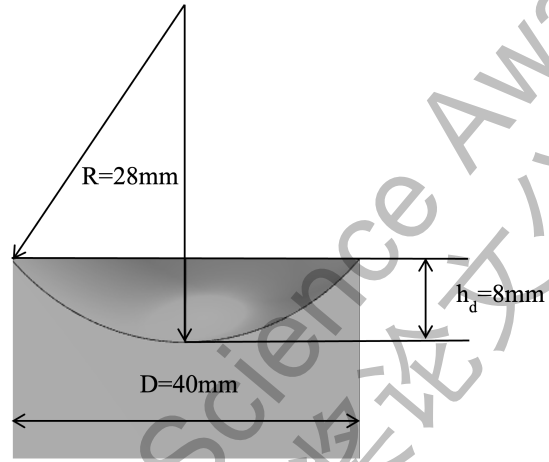


Figure 9: Concave Reflector Geometry Diagram

The tracking system, combined with carefully controlled lighting, provided the necessary data for the analysis of rotational dynamics

## 2.2 Tracker Configuration

The high-speed videos were imported into the **Tracker** software, which allowed us to measure a variety of experimental variables, including the position coordinates of the spheres, their angular displacement, and the rotational velocity. Once the initial data were extracted, further analysis was conducted using Excel and Origin Pro to determine the relationships between different experimental variables.

First, the spherical samples were labeled and organized in separate columns within a plastic mesh organizer. For tracking purposes, two crosses were marked on opposite sides of each sphere using thin-tip colored pens (one red and one blue). With the ultrasonic generator and reflector slightly misaligned, the high-speed camera captured the points where the samples could be levitated and rotated. The video was then imported into Tracker for analysis. A calibration stick, measuring  $4.00 \times 10^{-2}$  m on the diameter of the concave reflector, was used for precise scaling. Tape measures were applied to determine the vertical difference between the



Figure 10: 3-D Platform

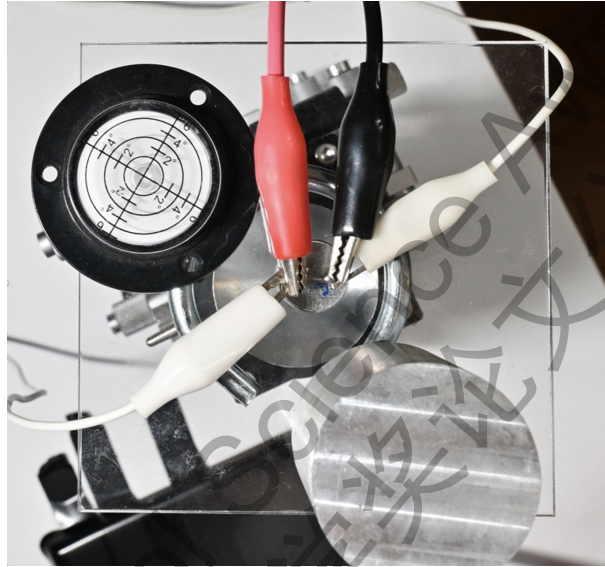


Figure 11: Level Adjustment

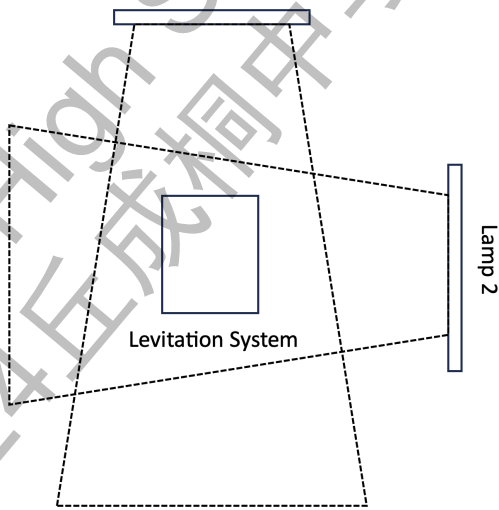


Figure 12: Lighting System

reflector and transducer, as well as the horizontal displacement of the reflector.

## 2.3 Simulation Configuration

MATLAB is a high-level programming environment used for numerical simulation, data analysis, etc., offering powerful tools for simulating complex systems with customizable code. COMSOL Multiphysics is also a simulation software that integrates various physical models using finite element analysis (FEA) to couple complex physical fields. We used these 2 softwares to explain the phenomenon in our experiments and also to provide theory analytical directions.

The main purpose of MATLAB in this study is to test the basic regularity of COMSOL simulations. Both MATLAB and COMSOL use similar ground theories to simulate acoustic fields. To verify the regularity of COMSOL directly is challenging, because of its complex Multiphysics approach, which couples multiple physical fields and solves them using finite element analysis. One drawback of COMSOL is its limitation of programmability compared to MATLAB. On the other hand, MATLAB is code-based, giving more room for customization and control over manipulating parameters. However, code-based simulation is more difficult for simulating the coupling of multiple physics fields due to programming difficulties and code efficiency. While in COMSOL we can use modules.

By using MATLAB to validate the regularity of COMSOL, we ensure that the foundational acoustic behavior is correct, making it possible for COMSOL to simulate more complicated physics fields. This cross-validation strengthens the reliability of our simulation results and provides a robust framework for understanding the dynamics of levitated particles in asymmetric acoustic fields.

## 2.4 MATLAB Approximation Model

To complement the experimental observations, a simulation of the acoustic levitation system was conducted using MATLAB. The simulation was based on the **Matrix Method for Acoustic levitation** [2] which modeled acoustic levitation systems involving ultrasonic transducers and reflectors. For this study, we focused on a system with a single reflector and ultrasonic transducer to simulate the relevant acoustic field behavior.

This Matrix Method leveraged the Rayleigh integral, which divides the transducer and reflector into multiple small cells (shown in Figure 13). The total sound

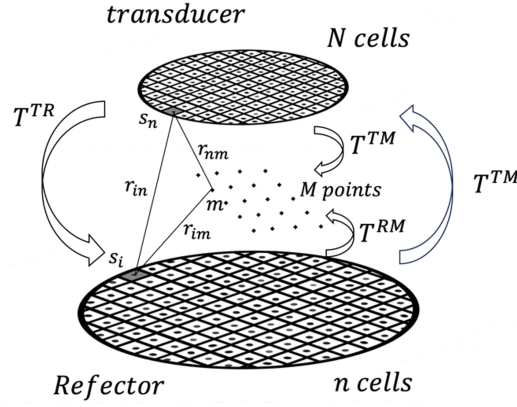


Figure 13: simulation Method Diagram

pressure at any designated point in space is calculated as the sum of contributions from these individual elements. To accurately describe the interaction between these cells, four matrices were generated.

$T_{TM}$  : The transfer matrix from the transducer to the measurement points.

$T_{RM}$  : The transfer matrix from the reflector to the measurement points.

$T_{TR}$  : The transfer matrix from the transducer to the reflector.

$T_{RT}$  : The transfer matrix from the reflector back to the transducer.

By initially neglecting the reflections between the transducer and the reflector, the direct pressure generated by the transducer at measurement point  $M$  in the acoustic field is expressed as

$$\begin{bmatrix} p_1 \\ p_2 \\ \vdots \\ p_M \end{bmatrix} = \frac{\omega \rho c}{\lambda} \begin{bmatrix} T_{11}^{(TM)} & T_{12}^{(TM)} & \cdots & T_{1N}^{(TM)} \\ T_{21}^{(TM)} & T_{22}^{(TM)} & \cdots & T_{2N}^{(TM)} \\ \vdots & \vdots & \ddots & \vdots \\ T_{M1}^{(TM)} & T_{M2}^{(TM)} & \cdots & T_{MN}^{(TM)} \end{bmatrix} \begin{bmatrix} U_1 \\ U_2 \\ \vdots \\ U_N \end{bmatrix} \quad (1)$$

Here,  $\mathbf{P} = [p_1, p_2, \dots, p_M]^T$ , represents the matrix containing all the acoustic pressure values at each measured point  $m$ .  $\omega$  is the angular frequency,  $\rho$  is the density of the propagation medium,  $c$  is the wave propagation velocity,  $\lambda$  represents the wavelength, and the elements of matrix  $\mathbf{T}^{(TM)}$  are given by [6] [1]. Similarly,

$\mathbf{T}^{(\text{TR})}$ ,  $\mathbf{T}^{(\text{RT})}$ , and  $\mathbf{T}^{(\text{RM})}$  are similar.

$$T_{mn}^{(\text{TM})} = s_n \frac{\exp(-jkr_{nm})}{r_{nm}}, \quad (2)$$

$$T_{in}^{(\text{TR})} = s_n \frac{\exp(-jkr_{in})}{r_{in}}, \quad (3)$$

$$T_{ni}^{(\text{RT})} = s_i \frac{\exp(-jkr_{in})}{r_{in}}, \quad (4)$$

$$T_{mi}^{(\text{RM})} = s_i \frac{\exp(-jkr_{im})}{r_{im}}. \quad (5)$$

Here,  $k = \frac{\omega}{c}$  represents the number of waves;  $j = \sqrt{-1}$ . The matrix given in Equation 1 is the same as the Rayleigh integral. When the transducer is emitting acoustic waves, the constant  $\frac{\omega\rho c}{\lambda}$  in Equation 1 should be used. The  $\frac{\omega\rho c}{\lambda}$  should be replaced by  $\frac{j}{\lambda}$  when the acoustic wave is reflected by the reflector and reaches the transducer. [7] [8]. The multiple reflections in the system are considered and calculated by adding the reflection terms to Equation 1. This gives us:

$$\begin{aligned} \mathbf{P} = & \left(\frac{\omega\rho c}{\lambda}\right) \mathbf{T}^{(\text{TM})} \mathbf{U} + \left(\frac{\omega\rho c}{\lambda}\right) \left(\frac{j}{\lambda}\right) \mathbf{T}^{(\text{RM})} \mathbf{T}^{(\text{TR})} \mathbf{U} \\ & + \left(\frac{\omega\rho c}{\lambda}\right) \left(\frac{j}{\lambda}\right)^2 \mathbf{T}^{(\text{TM})} \mathbf{T}^{(\text{RT})} \mathbf{T}^{(\text{TR})} \mathbf{U} \\ & + \left(\frac{\omega\rho c}{\lambda}\right) \left(\frac{j}{\lambda}\right)^3 \mathbf{T}^{(\text{RM})} \mathbf{T}^{(\text{TR})} \mathbf{T}^{(\text{RT})} \mathbf{T}^{(\text{TR})} \mathbf{U} \\ & + \left(\frac{\omega\rho c}{\lambda}\right) \left(\frac{j}{\lambda}\right)^4 \mathbf{T}^{(\text{TM})} \mathbf{T}^{(\text{RT})} \mathbf{T}^{(\text{TR})} \mathbf{T}^{(\text{RT})} \mathbf{T}^{(\text{TR})} \mathbf{U} + \dots \end{aligned} \quad (6)$$

The first term on the right-hand side corresponds to the direct pressure field emitted by the transducer, while the second term corresponds to the acoustic wave reflected by the reflector. Subsequent terms represent higher-order reflections within the system. 6 is equivalent to the numerical model Kozuka and collaborators proposed, in which the multiple reflections are considered by many Rayleigh integrals.

Given practical constraints such as experimental error and the computational capacity of the machine used (MacBook Air M2, 8GB RAM), we limited the simulation to the first four terms of the reflection series and neglected higher-order reflections for computational efficiency.

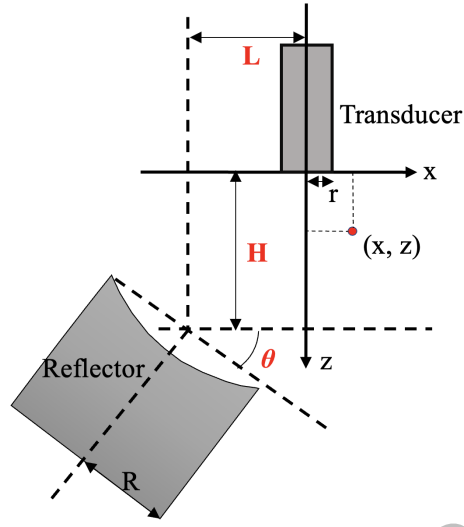


Figure 14: Parameter Diagram

The simulation parameters used in the simulation were carefully calibrated to match the experimental conditions (see Figure 14). Such as the ability to simulate scenarios where the reflector was translated both vertically and horizontally and tilted by an angle  $\theta$ . These simulations provided a clear representation of the sound pressure field, allowing us to identify the regions of the field responsible for generating rotational torque on the spheres.

In MATLAB simulations, the sagittal height and the vertical distance between the transducer's lower surface and the plate's top surface must be considered. Thus, the sound pressure field at a given height  $H$  is given by:

$$\text{Sound Pressure Field at } H = H' + s + d', \quad (7)$$

where  $H'$ : experimentally observed height (sagitta and the vertical distance between the lower surface of the transducer and the top surface of the plate neglected),  $s$ : sagitta, and  $d'$ : the vertical distance between the lower surface of the transducer and the top surface of the plate.

Using the sagitta  $s = r - \sqrt{r^2 - (\frac{c}{2})^2} = 5.38$  mm, and by using a micro screw gauge,  $d' = 8.40$  mm. Thus, the total Sound Pressure Field at  $H$ , accounting for both the sagitta and the vertical distance, is calculated to be 13.78 mm.

The verification of the regularity of MATLAB simulation is presented in Section 3.1.

## 2.5 COMSOL Modelling and Regularity Discussion

While MATLAB was used to develop a simplified model of the system, COMSOL Multiphysics provided a more detailed simulation of the acoustic field. COMSOL's ability to couple multiple physical fields, e.g., acoustic pressure field, velocity field, etc., allowed us to simulate the interaction between the acoustic pressure field and the levitated particles with higher accuracy than MATLAB.

The COMSOL model was constructed to mirror the experimental setup as closely as possible. The equation used to simulate the acoustic pressure field is shown in equation 8, (Frequency Domain Perturbation) is shown in equation 11. Figure 15 shows the geometric configuration of the transducer and reflector. By adjusting these parameters, we could fine-tune the simulation to match the experimental conditions and investigate how different configurations of the system affected the behavior of the levitated spheres.

$$-\frac{1}{\rho_c} \nabla^2 p_t - \frac{k_{eq}^2}{\rho_c} p_t = 0 \quad (8)$$

$$p_t = p + p_b \quad (9)$$

$$k_{eq}^2 = \left( \frac{\omega}{c_c} \right)^2 \quad (10)$$

$$-\mathbf{n} \cdot \left( -\frac{1}{\rho_c} \nabla p_t \right) = 0 \quad (11)$$

In equation 8,  $\rho_c$  represents the compressibility-related density of the medium,  $\nabla^2 p_t$  is the Laplacian of the total pressure  $p_t$ , and  $k_{eq}^2$  is the square of the equivalent wave number related to the system's angular frequency and speed of sound. In equation 9,  $p_t$  represents the total pressure, which is the sum of the static pressure  $p$  and the background pressure  $p_b$ . In Equation 10 where  $\omega$  is the angular frequency and  $c_c$  is the speed of sound in the medium. In Equation 11,  $\mathbf{n}$  is the unit normal vector to the boundary,  $\nabla p_t$  is the gradient of the pressure, and  $\rho_c$  is the compressibility-related density, ensuring that the pressure flux across the boundary is zero.

To discuss the regularity of the COMSOL simulation results, we compared the acoustic pressure field simulated in both software. Under the parameter of  $H = 20$  mm, it is apparent that simulated acoustic pressure results from COMSOL (Figure

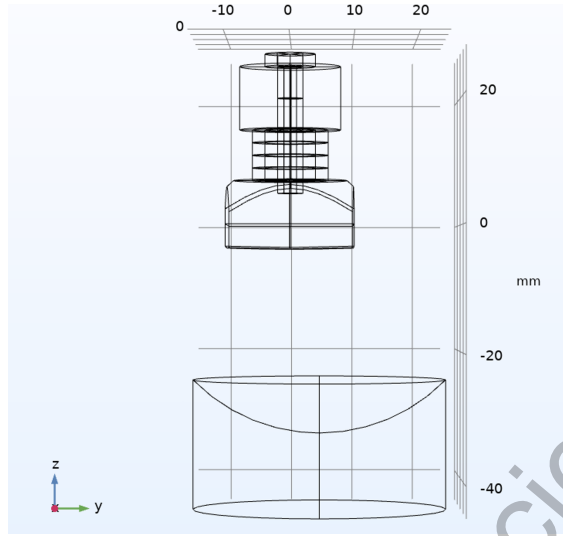


Figure 15: COMSOL Geometry Configuration

16) and MATLAB (Figure 17) are highly consistent (field shape, number of nodes). This is shown from the number and distribution of nodes present. Nodes are key indicators of the wave properties such as wavelength and frequency. The distribution of nodes reflects how the pressure field behaves across the system. If the number of nodes matches in both simulations, this shows that the pressure variations are being modeled consistently. Further evidence is shown in Figure 18, showing the position of the local minima, validating the regularity of COMSOL.

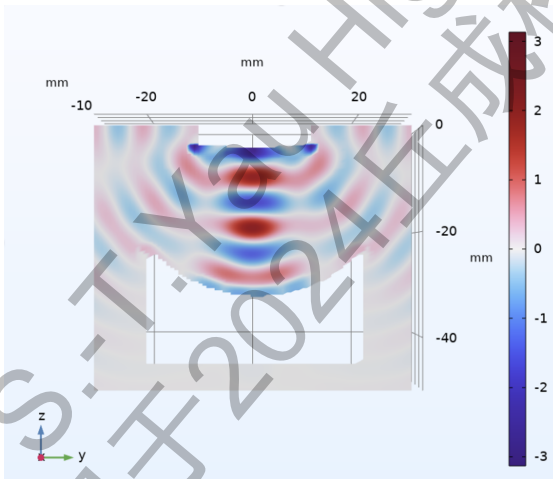


Figure 16: COMSOL Simulation At  $H = 19.82\text{mm}$

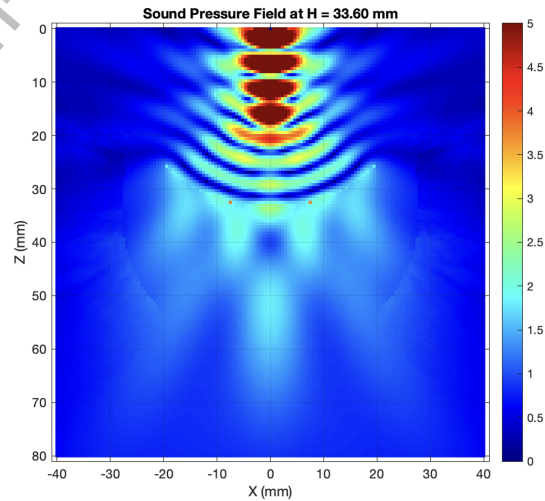


Figure 17: MATLAB Simulation At  $H = 19.82\text{mm}$

The combined use of MATLAB and COMSOL allowed us to obtain both a simplified understanding of the system (via MATLAB) and a detailed, Multiphysics

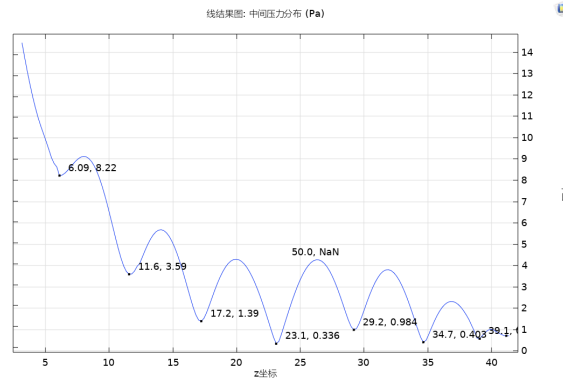


Figure 18: COMSOL Local Minima At H=19.82mm

simulation (via COMSOL). This dual approach ensured that the simulation results were robust and reliable across different platforms.

## 3 Experimental Data and Numerical Simulation Results Analysis

With the experimental setup and simulations fully described, the next step involves a detailed comparison of the **experimental data** and the **numerical simulation results**. By analyzing the rotational behavior of levitated spheres in both symmetric and asymmetric acoustic fields, we aim to uncover the underlying relationships between the applied voltage and angular velocity of the spherical sample which implies the strength of the sound pressure field.

### 3.1 Validation of MATLAB Simulation

In this section, the accuracy of MATLAB simulation is validated by comparing the simulated local minima of the acoustic pressure field with the z-coordinates of the levitated sphere in the experiment. The slight discrepancy between reality and simulation is mentioned as well.

To ensure a symmetric field, we aligned the axis of the transducer with the reflector, eliminating any horizontal offset. By systematically varying the vertical distance  $H$  between the transducer and reflector, we modified the acoustic field between them. The resulting standing wave patterns were then analyzed alongside the corresponding MATLAB simulation results (Figure 27).

In the simulation, we focused on the central axis of the transducer and reflector. By extracting the local minima of the acoustic pressure field along the axis, we were able to plot the theoretical Z-coordinate of the levitated sphere. These theoretical values were then compared with the experimental data obtained from Tracker software. As illustrated in Figure 21, the experimental data closely aligns with the simulated results, validating the regularity of the MATLAB code.

(Note: In MATLAB, we simulate the system in 2D, where the experimental Z-coordinate is equivalent to the simulation's Y-axis. Only  $H = 0$  mm to  $H = 36.60$  mm is valid)

While the overall agreement between the simulation and experimental data is strong, some discrepancies were noted in specific instances. However, in simulation,

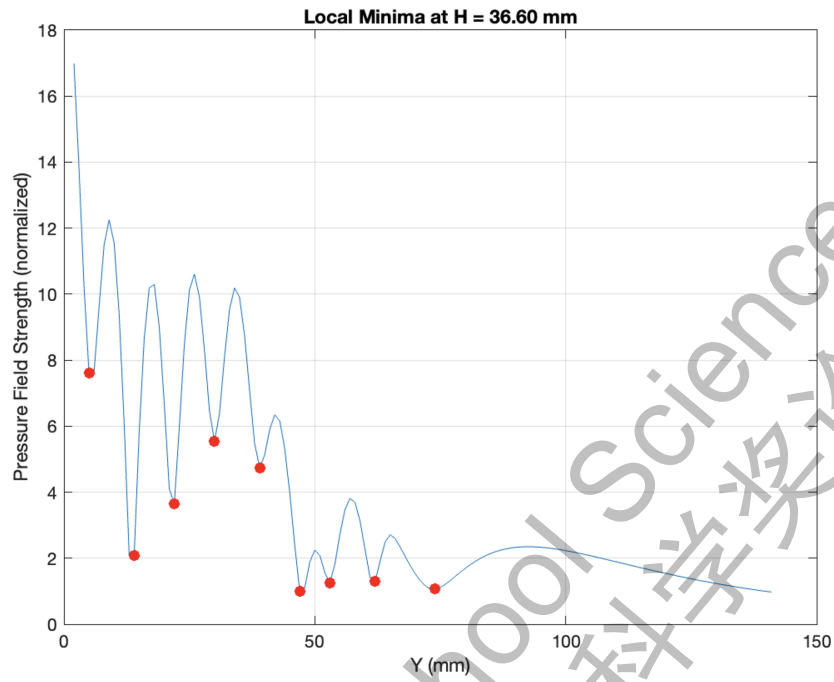


Figure 19: Local minima of the acoustic pressure field at  $H = 22.81$  \*

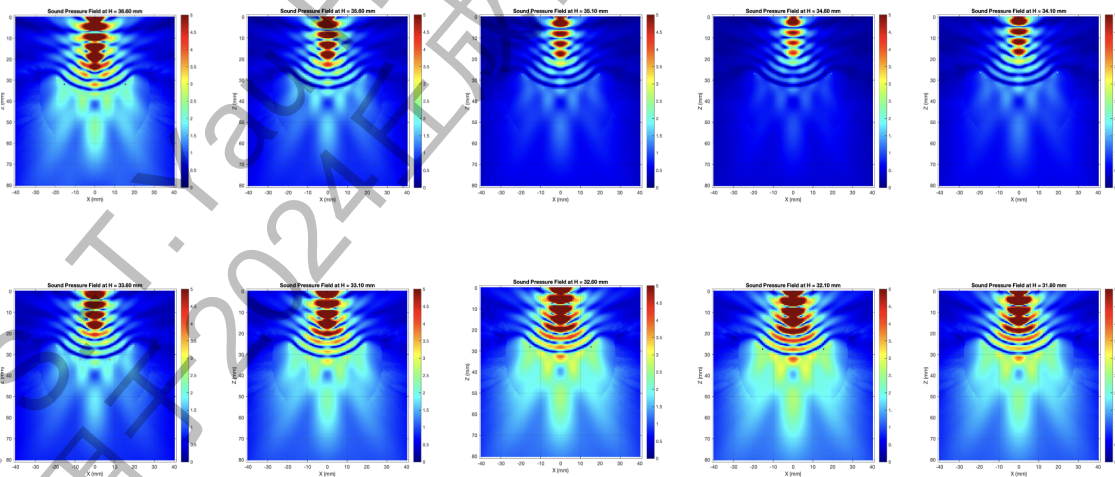


Figure 20: MATLAB simulation results showing the acoustic pressure minima at varying distances from  $H = 22.81$ mm to  $H = 19.81$ mm. (x-axis represents the X-offset, y-axis represents the height  $H$ ).

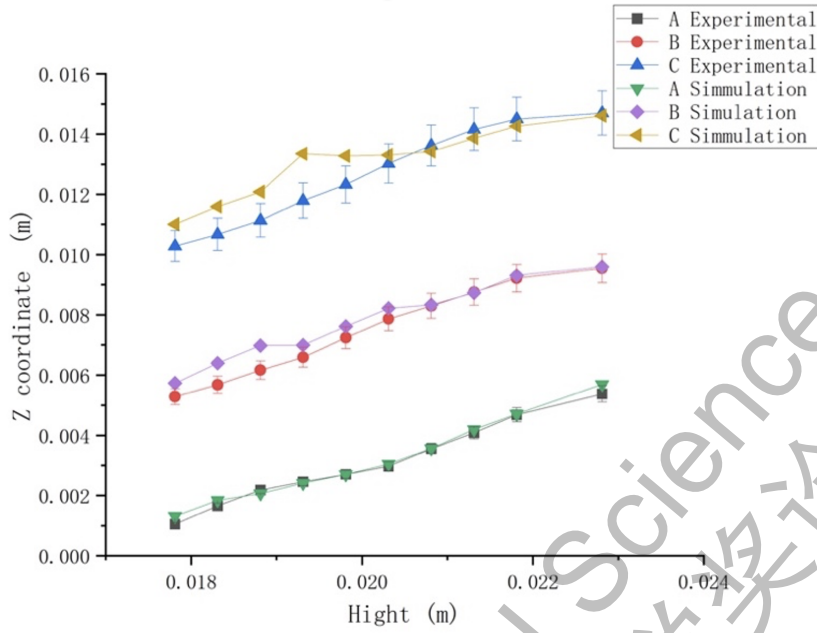


Figure 21: Comparison between theoretical and experimental values of (vertical distance between transducer and reflector) and (position of the levitated sphere).

the scenario is very ideal. These fluctuations may be attributed to various factors, including the influence of gravity on the levitated particles, as suggested by [10]. Further investigation into the effects of gravitational forces, as well as potential experimental uncertainties, could help clarify these discrepancies.

Despite these minor differences, the regularity of the MATLAB simulations is successfully demonstrated. Our results confirm that the levitated sphere consistently occupies local minima of the acoustic pressure field which could refer to potential well [13][5]

### 3.2 Relationship between Applied Voltage and the Angular Velocity of Polystyrene Spheres (with fixed X-offset)

The primary aim of this section is to investigate the relationship between input voltage and the angular velocity of levitated polystyrene spheres. Additionally, we sought to determine whether any acceleration phenomenon could be observed during the experiment.

In this experimental group, we focused on the angular velocity of the levitated and rotating polystyrene spheres. To maintain consistency, the vertical height and

horizontal offset of the reflector were kept constant throughout the experiment. We first varied the applied voltage from 55 V to 20 V, decreasing the voltage in 5 V reduction. After that, another transducer is employed and the angular velocity change relative to voltage under different X-offset is measured and calculated.

The reason for starting at 55 V is due to the limitations of the camera's frame rate, which has a maximum of 120 frames per second (fps). At a voltage above 55 V, the angular velocity of the rotating spheres exceeded the camera's ability to capture a full rotation within one frame cycle. As a result, there was insufficient data between frames, leading to inaccurate analysis. Consequently, we limited the voltage to 55 V and below to ensure that the camera would capture sufficient footage for reliable analysis.

To determine the angular velocity, we used the protractor tool in **Tracker** (as shown in Figure 22). For each frame, we tracked the identifier on the rotating sphere and measured the angle between its position in the current frame and the previous one. This process was repeated across 10 frames. The total angular displacement across the 20 frames was then summed, and the angular velocity was calculated by dividing the total angular displacement by the time interval,  $20 \times dt$ , (where  $dt = 8.34 \times 10^{-3}$  s).

The table below (Table 1) presents the angular velocities corresponding to different voltage inputs: We employed the protractor tool in Tracker (shown in Figure 22

Table 1: Average Angular Velocity at Different Voltage Levels

Voltage (V)	Angular Velocity (rad/s)
20	104.56
25	153.46
30	183.08
35	222.10
40	243.98
45	278.78
50	303.34
55	324.11

), after tracking down the identifier in every frame, we measured and recorded the angle between the identifier in the current frame and the former frame then moving on to the next frame. This process is repeated for 20 different frames. After that, we summed up the total angles covered for 20 frames, then divided it by 10 times the time difference between frame  $dt$  ( $8.34E-3$  s).

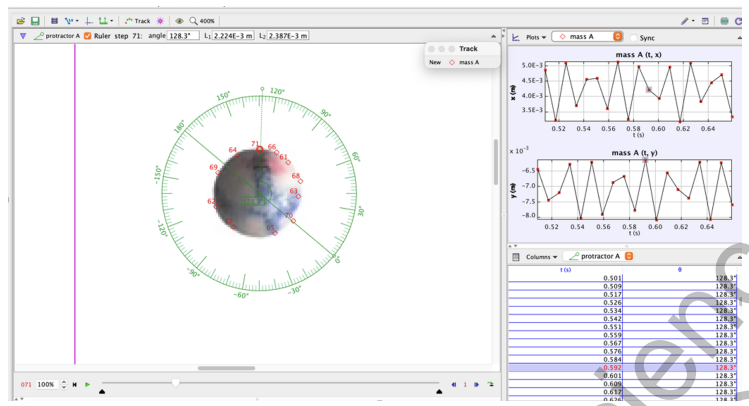


Figure 22: Protractor used in Tracker Example

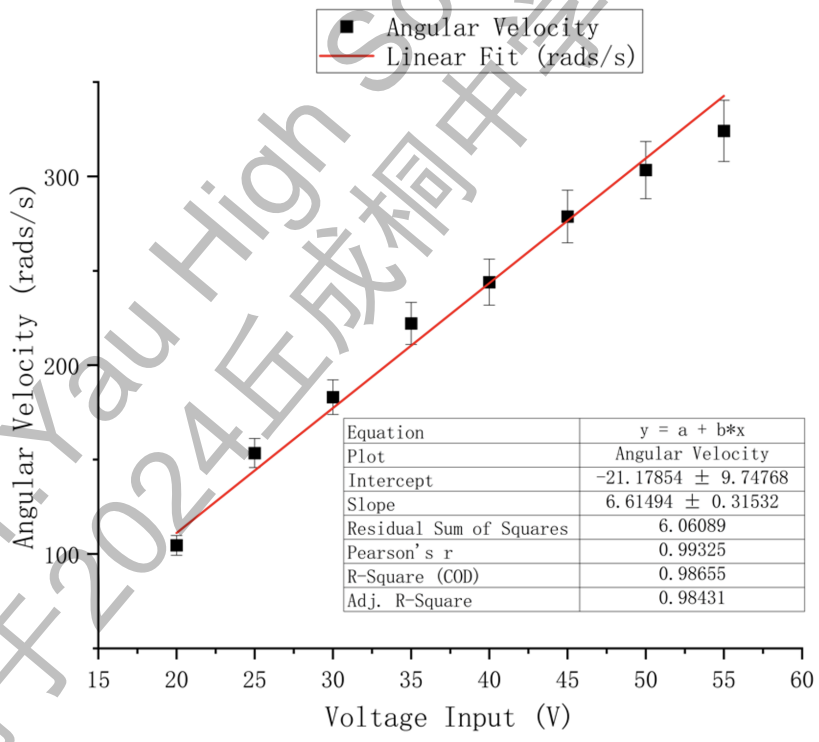


Figure 23: Linear Fit of Voltage vs Angular Velocity for Polystyrene Spheres at  $H=1.973E-2$ ,  $L=5.612E-3m$

After plotting the results, we performed a linear fit of the data, as shown in Figure 23. The linear fit yielded an  $R^2$  (coefficient of determination) value of 0.98655, which is very close to 1. This indicates a strong linear relationship between the applied voltage and the angular velocity of the levitated spheres.

The linear fit equation can be expressed as:

$$\omega = aV + b$$

Where:

- $a = 6.61494 \pm 0.3152$  is the slope, indicating the rate of change of angular velocity with respect to voltage.
- $b = -21.17583 \pm 9.74768$  is the intercept.

The percentage errors for the slope and intercept are 4.765% and 46.03%, respectively. These values indicate the level of uncertainty in the fit parameters, with the intercept showing greater variability due to the high percentage error.

The strong linearity between the applied voltage and the angular velocity suggests that the angular velocity ( $\omega$ ) of the sphere is directly proportional to the square of the applied voltage ( $P \propto V^2$ ).

To further verify the linearity observed in Figure 23, we took the natural logarithm of both sides of the equation. The resulting plot Figure 24 yielded a slope close to 1, confirming the linear relationship between the applied voltage and angular velocity. Taking the logarithmic transformation allowed us to confirm that the voltage input scales logarithmically with the angular velocity, providing additional support for the linear fit.

Unfortunately, we did not observe any significant acceleration phenomenon in either the experimental data or the Tracker analysis. This may be due to the rapid change in velocity, which occurred too quickly for the camera to capture in real-time.

Although the acceleration phenomenon was not captured in this experiment, the strong linear relationship between the voltage input and angular velocity provides a clear understanding of the effects of acoustic radiation power on the rotational

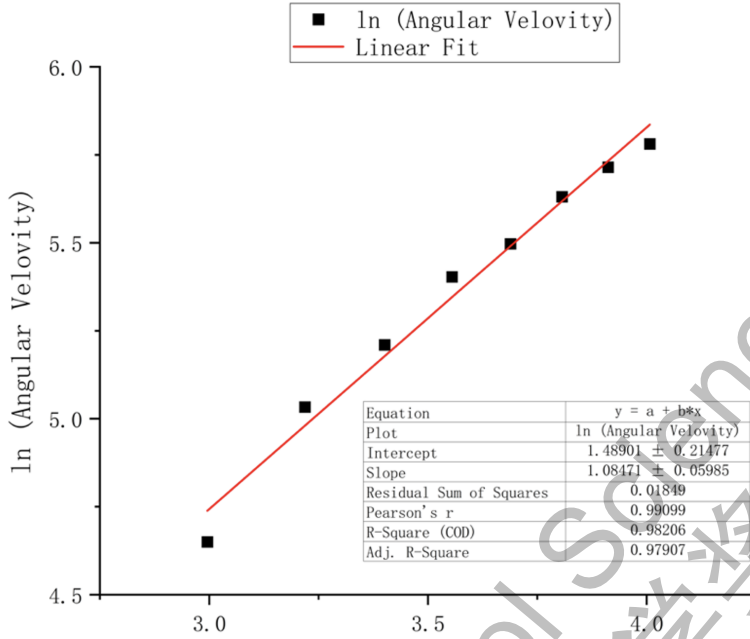


Figure 24: Logarithmic Plot of Angular Velocity vs Voltage

dynamics of levitated spheres. This understanding forms the basis for further investigations into the behavior of the system under asymmetric acoustic fields.

### 3.3 Relationship between the X-offset of the Reflector and the Rotating Sphere's Angular Velocity

In order to test the relation between the horizontal offset and the acoustic radiation torque, a set of experiments are conducted with a different horizontal offset between the center axis of the transducer and the reflector. Throughout all the experiments with different horizontal offset setups, the spherical samples are levitated nearly at the same point with respect to the center of the reflector. The angular velocity at different input voltages of the transducer is recorded. As mentioned above, the relationship between the angular velocity and the input voltage is revealed to be linear, while the slope and  $R^2$  values are calculated. The R-squared shows that the expected linear relationships are all solid. As the horizontal offset increases, the angular velocity is expected to decrease, however, according to the data, it first increases and then decreases. The reason seems to be simple, with a small horizontal offset, the asymmetry of the acoustic field is just established and the acoustic radiation torque at the levitated point is small. As the horizontal offset increased, the asymmetry of the acoustic field kept increasing and reached its peak

at nearly 5.22 mm. Finally, as the horizontal offset increases, the focus effect of the reflector decays rapidly as well as the acoustic radiation pressure.

Table 2: Relationship Between X-offset and H with Various Slope and R-squared Values

X-offset (mm)	H (mm)	Slope of angular velocity - output voltage	R squared of X-offset - H	Ln slope	R squared of Ln graph
2.224	18.48	7.92	0.9617	0.8729	0.9622
2.752	18.52	8.62	0.9807	1.220	0.9926
2.789	18.47	10.93	0.9931	1.017	0.9800
4.490	18.58	14.61	0.9782	1.150	0.9894
5.220	18.65	15.75	0.9703	1.150	0.9894
5.620	18.53	12.05	0.9930	0.8588	0.9620

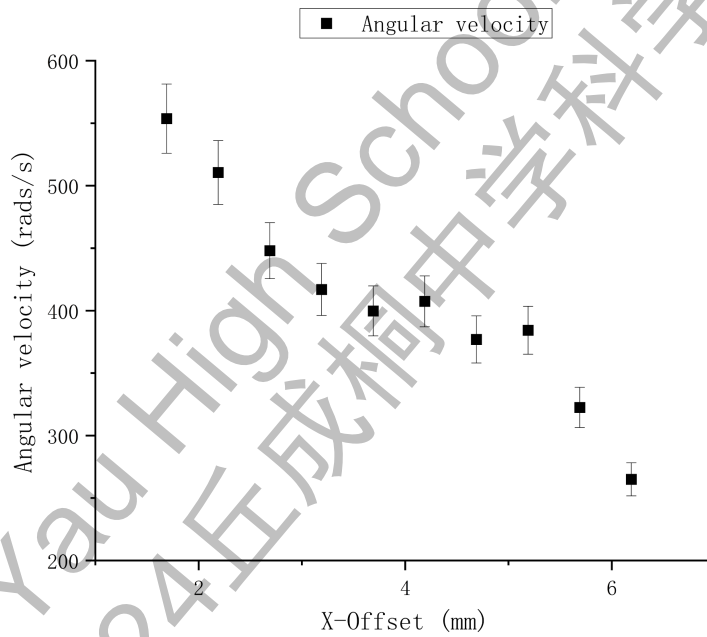


Figure 25: Angular Velocity - X-offset under 55V.

Then, another experiment are conducted in a dynamic way: the spin situation of the spherical sample was recorded as the reflector kept moving away from the center of the symmetric axial of the transducer. On the moving of the reflector, we stopped at several positions to see if the angular velocity of the spherical sample reached a stable value. The spherical sample reached uniform spin at every stop position as a result of the balance embellishment between the acoustic radiation torque and the air resistance torque. And the terminal angular velocity represents the level of the acoustic radiation torque at the levitated point. The result is shown

in the Figure 25, and the angular velocity decreased as the reflector kept moving away, which reveals that the focus of the acoustic field is weaker as the reflector kept moving away from the transducer. But in this process, no peak values are found in the middle of the experiment or at 5.22 mm. The reason can be simple—the slope between the input voltage and the angular velocity represents the sensitivity of the power input to the acoustic torque, but the absolute value can be calculated with slope and y-intercept. The y-intercept may be large in the later experiment because of measurement uncertainty and larger background sound pressure.

2024 S.-T. Yau High School Science Award  
仅用于2024丘成桐中学科学奖论文公示

## 4 Discussion

The phenomenon investigated is novel, to the best of our knowledge. Recent studies on spinning angular momentum primarily focus on the use of multiple transducers (typically two or more) with set phase differences to generate a spinning effect. However, our experiment reveals that the spinning behavior of levitated particles can be induced by the change of the axisymmetric acoustic field into the asymmetric field. This unique approach to creating rotational motion unveils a new aspect of the properties of acoustic fields and dynamics of levitated objects, opening potential avenues for further investigation.

This discussion is divided into several key areas: the theoretical analysis of rotating spheres, the parameters influencing the angular velocity of spheres, and error analysis in both experiments and theoretical contexts.

### 4.1 Theory Discussion

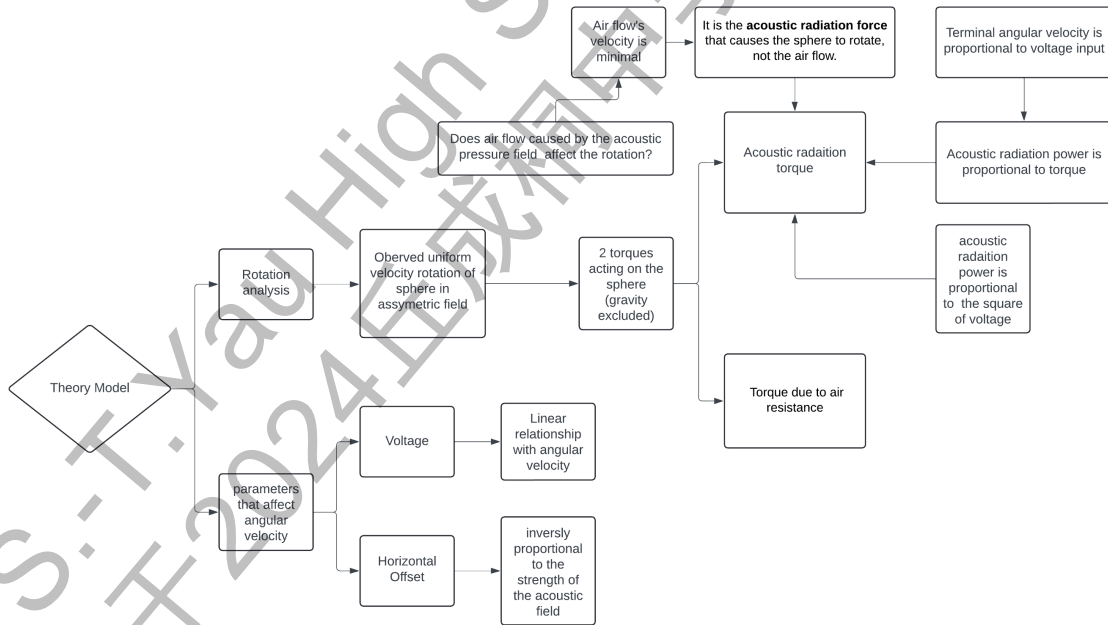


Figure 26: Theory Model Flowchart.

Here in Figure 26 is a flowchart illustrating our theoretical model, which provides the framework for the following discussions in this research.

#### 4.1.1 Torques Acting on the Rotating Sphere

In our experiments, no rotational motion around a fixed horizontal axis was observed when there was no horizontal displacement of the reflector. However, irregular objects revolving around a vertical axis were noted, consistent with the water droplet rotation phenomenon described in previous studies [15]. From this observation, we hypothesize that the acoustic field generates an acoustic radiation torque on the levitated object, initiating its rotation.

Through analysis using **Tracker**, we found that the sphere in all of our experiments eventually reached a constant angular velocity. This behavior is analogous to a car traveling through air and eventually reaching terminal velocity. In this case, the condition for a steady rotational state occurs when the acoustic radiation torque accelerating sphere is balanced by opposing air resistance torque, achieving terminal angular velocity.

To explore this further, we conducted experiments maintaining a fixed horizontal and vertical offset while gradually decreasing the voltage using a power amplifier. The stability of the sphere's rotation indicated that the acoustic field structure remained intact. Conversely, changes in angular velocity as we varied the voltage suggested a direct relationship between acoustic radiation force and terminal velocity. These changes imply that the torques acting on the sphere are sensitive to the power of the acoustic field, which directly depends on the input voltage.

Our final results show a high degree of linear correlation between the input voltage and terminal angular velocity, with coefficients of determination ( $R^2$ ) of 0.988 and 0.9905 for two experimental groups. This linear relationship suggests that the acoustic radiation power is proportional to the square of the input voltage ( $P \propto V^2$ ), and torque ( $\tau$ ) acting on the object is proportional to the acoustic radiation power (Figure 27). This relationship supports the hypothesis that:  $P \propto \tau$ , and  $P \propto V^2$ .

Air resistance, in comparison, is proportional to the square of the relative velocity. This relationship further suggests that the ultrasonic input voltage is linearly related to the terminal angular velocity. Using classical fluid dynamics models, we can calculate the torque due to air resistance as:

$$\tau = \frac{1}{2} C_d \rho A v^2 L \quad (12)$$

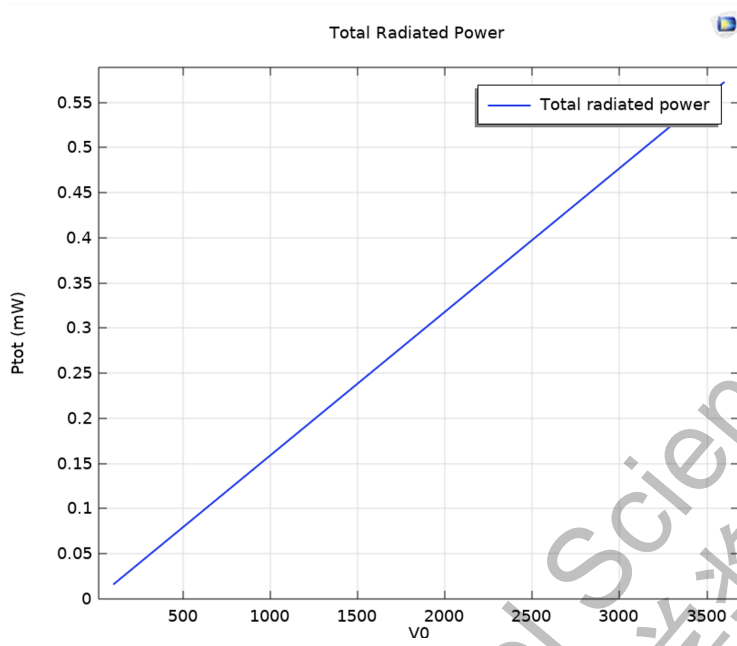


Figure 27: Total Radiated Power – The square of Voltage.

where  $C_d$  is the drag coefficient,  $\rho$  is the air density,  $A$  is the cross-sectional area,  $v$  is the velocity of the object relative to air, and  $L$  is the moment arm. This equation explains how air resistance grows with velocity and acts to limit the rotational speed of the levitated sphere. In our system, the balance between the acoustic radiation torque and the air resistance torque ultimately determines the sphere's steady rotational speed. (This equation may not be suitable in our scenario.)

#### 4.1.2 Discussion on the Existence of Torque

As discussed earlier, the spherical sample can be levitated in an asymmetric acoustic field maintaining a uniform speed rotation. We consider there are two possible mechanisms behind this process. First, the rotation of the spherical sample may be led by the rotated air flow created by the acoustic field. To test this hypothesis, we constructed a local air particle vector field using COMSOL. The vector field is calculated by Equation 13.

$$\vec{v} = -\frac{\nabla p}{i\omega\rho_0} \quad (13)$$

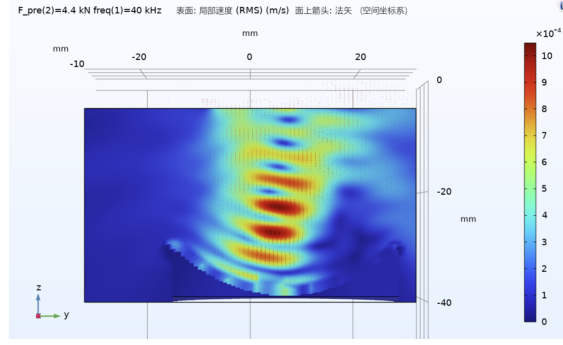


Figure 28: local air particle vector field.

where  $\vec{v}$  is the particle velocity,  $\nabla p$  is the pressure gradient,  $i$  is the imaginary unit,  $\omega$  is the angular frequency, and  $\rho_0$  is the ambient density of the medium. The acoustic pressure field  $p$  can be calculated using Equation 1 as mentioned before.

The RMS presented in the diagram is the root mean square of the local velocity field, whose absolute value is small where the most intense part only reaches  $10^{-4}$ .

The simulation results are given in Figure 28. Angular velocity (of the edge of the spinning sphere) in experiments ranges from 0.11424 m/s to 0.84 m/s (converted to linear velocity). However, the color bar in 28 shows a magnitude of the local air particle velocity on the order of  $10^{-4}$ , while in experimental data, the velocity is on the order of  $10^{-1}$ . These two magnitudes are not in the same range, confirming that the movement of local air can be considered to be stationary compared to the spinning sample. Therefore, there must be an air resistance.

Thus, we conclude that spin angular momentum is primarily caused by the distorted shape of the pressure field. This distortion arises from the interaction between the standing sound wave, affected by the X-axis offset of the reflector and the transducer. The asymmetry in the pressure field likely triggers the spinning by uneven acoustic radiation torque which may accelerate the rotation of the sample. As the rotation accelerates, the sample's rotation reaches a stable state with a terminal angular speed as a result of the balance between the acoustic radiation torque and the air resistance torque.

One possible explanation of the origin of the acoustic radiation torque is that the levitated sphere remains trapped in the potential well while the waves from the transducer and reflected waves provide different directions of acoustic radiation force, adding up to non-zero torque. At the same time, the sphere is still trapped in the node, resulting in a spinning phenomenon. Supporting evidence for this

explanation includes consistent observation of levitated spheres following a similar path – moving upward and away from the transducer – each time they left the node. This indicates that the pressure at the node where the spheres are levitated fails to counteract the acoustic radiation force from the reflector, further confirming the pressure field’s role in generating the observed spinning behavior.

#### 4.1.3 Factors Affecting Angular Velocity

Understanding the origin of the torque that drives rotation naturally leads to examining the factors that influence the sphere’s angular velocity. Among these, the input amplitude and the X-offset of the reflector are particularly significant. The input amplitude directly affects the strength of the acoustic field, while the X-offset alters the field’s symmetry and intensity. Our experimental results indicate that increasing the X-offset requires a higher minimum amplitude to sustain levitation at a given node. This is likely due to the way the X-offset disrupts the balance of forces within the acoustic field, distorting the pressure field and reducing the efficiency of levitation.

These findings align with previous research, such as that by M. Barmatz and colleagues[20], which demonstrated that the levitation capabilities of an acoustic field depend heavily on its geometric configuration. We observed that as the input amplitude approached its minimum threshold for levitation, further reductions caused the sphere to drop, regardless of how gradually the amplitude was reduced. This suggests that the acoustic pressure decreases rapidly as the sphere moves away from the pressure node, contrasting with the behavior of fluids, where pressure increases with depth. In the case of acoustic levitation, once the object begins to drift from the node, the forces maintaining levitation rapidly diminish, causing it to fall.

This sensitivity to both input amplitude and X-offset highlights the complex relationship between the geometry of the acoustic field and the rotational dynamics of the levitated sphere. By carefully controlling these parameters, we can influence not only the stability of levitation but also the angular velocity of the sphere, offering deeper insights into the mechanics of acoustic spin.

#### 4.1.4 The Effect of Gravity on the Equilibrium Axial Displacement of the Centre of the Spherical Sample

In Figure 21, we observed a discrepancy in the z-axis of the rotating sphere. The z-coordinates of local minima simulated by MATLAB are slightly higher than experimentally measured z-coordinates of the center of the sphere. This displacement aligns with the observations of Lierke and Holitzner, who proposed in their study, *Perspectives of an acoustic–electrostatic/electrodynamical hybrid levitator for small fluid and solid samples* [10], that the equilibrium axial displacement is influenced by gravity. The axial radial gradients from the pressure node, as given by equations 14 and 16, lead to normalized levitation forces along both axes:

$$F_{z,ac}(0, z) = -2k_z \cdot \sin(2k_z z) \quad (14)$$

$$F_{r,ac}(r, 0) = 2k_r \cdot \frac{4 \cdot J_1(k_r r)}{(k_r r)^2} \cdot \left[ J_0(k_r r) - \left( \frac{2 \cdot J_1(k_r r)}{k_r r} \right) \right] \quad (15)$$

$$\approx -\frac{k_r}{2} \cdot \sin(k_r r) \quad (16)$$

Using the axial levitation safety factor  $\Phi_s = \frac{1}{\sin(2k_z z)} > 1$  [4], and the weight of the sample  $m_s g_0 = \rho_s V_s g_0$ , we find from equations 14 and 16 that:

$$F_{z,ac}(0, z) \approx -m_s g_0 \Phi_s \cdot \sin(2k_z z), \quad (17)$$

$$F_{r,ac}(r, 0) \approx -\frac{1}{4} m_s g_0 \Phi_s \cdot q \cdot \sin(q \cdot k_z r), \quad (18)$$

$$\frac{F_{r,\max}}{F_{z,\max}} \approx \frac{q}{4}. \quad (19)$$

The equilibrium axial displacement of the sample's center from the pressure node is given by equation 20:

$$\Delta z = -\frac{\lambda_z}{4\pi} \cdot a \sin\left(\frac{1}{\Phi_s}\right) \leq -\frac{\lambda_z}{8} \quad (20)$$

which allows for a rough calibration of the levitation safety factor,  $\Phi_s$ .

As shown,  $\Delta z$  is related to  $g$ , and from this, we deduce that the experimentally

measured  $\Delta z$  values should be shifted downward to align with the simulated data.

However, in all of our experiments, the calibration is excluded with  $\lambda_z = \frac{c}{f} = \frac{343 \text{ m/s}}{40,000 \text{ kHz}} = 0.008575 \text{ m}$ ,  $\Delta z \leq -\frac{\lambda_z}{8} = -\frac{0.008575}{8} \text{ m} = 1.07 \times 10^{-3} \text{ m} = 1.07 \text{ mm}$ .

This decision was made for two reasons. First, while gravity introduces a measurable shift in the axial displacement, it was not significant enough to affect the primary focus of our study—understanding the rotational dynamics and behavior of the levitated particles under varying acoustic field parameters, especially voltage input and the X-offset, not the relative height of the sphere to the transducer.

Second, incorporating calibration for gravitational displacement would require a level of precision beyond the scope of our current experimental setup. In Equation 20,  $a$  represents the amplitude of the acoustic wave in our system, which is related to the voltage input. However, due to inherent limitations in the stability and precision of the experimental apparatus, the voltage input has approximately  $\pm 3\%$  to  $\pm 5\%$  of fluctuation. These unavoidable errors introduced by the apparatus potentially added unnecessary complexity.

## 4.2 Limitations

### 4.2.1 Measurements

Despite the limited frame rate of our camera (120 Hz), which made it challenging to analyze angular speeds as high as 700 rad/s, we developed a method to measure angular velocity using **Tracker** software. This method is sensitive to the angle of measurement, and while the manual counting of rotations introduces some errors, it remains within an acceptable range.

One significant factor affecting measurement accuracy is the angle of video recording. To minimize parallax error, we ensured that the camera was perpendicular to the spinning axis during the experiments. However, future experiments could benefit from using a higher frame rate camera and more accurate positioning of the camera relative to the spinning axis.

#### 4.2.2 Experimental Environment

Our experiments were conducted in a standard school physics laboratory that while relatively dry, clean and dust-free school, was not a fully controlled environment. The absence of a dedicated lab setup made it impossible to accurately control certain environmental that can affect our experimental results, such as ambient temperature, humidity, or airflow. Future work would greatly benefit from conducting experiments in a specialized lab where these variables can be tightly regulated, ensuring more consistent and accurate data collection.

2024 S.-T. Yau High School Science Award  
仅用于2024丘成桐中学科学奖论文公示

## 5 Summary

### 5.1 Conclusion

This study successfully investigated the rotational dynamics of levitated polystyrene spheres in asymmetric acoustic fields, employing a combination of experimental techniques and numerical simulations in a novel approach. Our novel approach revealed a strong linear relationship between the input voltage and the angular velocity of the rotating sphere, as demonstrated by the high coefficient of determination ( $R^2 > 0.98$ ). This supports the hypothesis that angular velocity has in linear relationship with applied voltage, confirming that acoustic radiation power is proportional to the square of the input voltage.

The phenomenon of the spheres reaching terminal velocity suggests the presence of two opposing torques: one generated by the distorted acoustic pressure field and the other by air resistance. The equilibrium between these forces explains the stabilization of the sphere's angular velocity.

Our investigation also explored whether local air velocity contributed to the rotational phenomenon. By comparing COMSOL simulations of the velocity field with experimental data from Tracker software, we found that the local air particle velocity was minimal compared to the sphere's rotational speed. This confirms that the acoustic radiation torque for the rotation originates from the acoustic pressure field rather than air movement. However, the air resistance appears when the rotational speed reaches a considerably high value and keeps increasing till the sample reaches terminal speed as a result of the balance of the acoustic radiation torque and air resistance torque.

The relationship between the X-offset and the distortion of the acoustic field is discussed through the experimental data of the X-offset and the angular velocity. The slope between input voltage and terminal angular velocity will firstly increase as the X-offset increases from zero and decreases after reaching a peak value at 5.22 mm. The reason can be the creation of the distortion of the acoustic field and the decreasing focus effect of the reflector as the X-offset increases.

## 5.2 Future Work

Building on the insights from this study, future research should aim to extend the current 2D analysis to 3D, which will allow a more comprehensive understanding of the rotational dynamics in asymmetric acoustic fields. This extension will enhance the generality and adaptability of the framework, making it applicable to a wider range of acoustic levitation systems and potential industrial applications.

Additionally, there is promising potential for coupling multiple physical fields—such as acoustic pressure, Gor'kov potential, and others—into a unified model. By integrating these fields, future research can develop more comprehensive simulations and analyses. This approach provides another degree of freedom to manipulate objects with zero contact, which benefits industries that rely heavily on the purity of the environment, such as high-temperature material processing, bioreactors, spin coating in chip manufacturing, and other fields requiring precise control in container-free environments. Unifying these models could pave the way for more efficient, accurate, and scalable applications of acoustic levitation in various scientific and industrial domains.

## References

- [1] Marco AB Andrade, Julio C Adamowski, Alberto Ibáñez, Montserrat Parrilla, and Carlos Fritsch. Optimization of complex shape part inspections with phased arrays. In *2009 IEEE International Ultrasonics Symposium*, pages 733–736. IEEE, 2009.
- [2] Marco AB Andrade, Nicolas Perez, Flavio Buiochi, and Julio C Adamowski. Matrix method for acoustic levitation simulation. *IEEE transactions on ultrasonics, ferroelectrics, and frequency control*, 58(8):1674–1683, 2011.
- [3] Shifang Guo, Zhen Ya, Pengying Wu, and Mingxi Wan. A review on acoustic vortices: Generation, characterization, applications and perspectives. *Journal of Applied Physics*, 132(21), 2022.
- [4] C Heinisch, J Petter, N Damaschke, T Tschudi, and C Tropea. An electrodynamic trap with an advanced geometry used for evaporation rate measurements of single water droplets. In *Proceedings of the 21th ILASS-Europe Meeting, Mugla, Turkey*, pages 10–13, 2007.
- [5] ZY Hong, JF Yin, W Zhai, N Yan, WL Wang, J Zhang, and Bruce W Drinkwater. Dynamics of levitated objects in acoustic vortex fields. *Scientific reports*, 7(1):7093, 2017.
- [6] A Ibáñez, C Fritsch, M Parrilla, and J Villazón. Monochromatic transfer matrix method for acoustic field simulation thorough media boundaries. *Physics Procedia*, 3(1):883–890, 2010.
- [7] Teruyuki Kozuka, Kyuichi Yasui, Toru Tuziuti, Atsuya Towata, and Yasuo Iida. Acoustic standing-wave field for manipulation in air. *Japanese Journal of Applied Physics*, 47(5S):4336, 2008.
- [8] Teruyuki Kozuka, Kyuichi Yasui, Toru Tuziuti, Atsuya Towata, Judy Lee, and Yasuo Iida. Measurement and numerical calculation of force on a particle in a strong acoustic field required for levitation. *Japanese Journal of Applied Physics*, 48(7S):07GM09, 2009.
- [9] Junfei Li, Alexandru Crivoi, Xiuyuan Peng, Lu Shen, Yunjiao Pu, Zheng Fan, and Steven A Cummer. Three dimensional acoustic tweezers with vortex streaming. *Communications Physics*, 4(1):113, 2021.

- [10] EG Lierke and L Holitzner. Perspectives of an acoustic-electrostatic/electrodynamic hybrid levitator for small fluid and solid samples. *Measurement Science and Technology*, 19(11):115803, 2008.
- [11] José H Lopes, Everton B Lima, José P Leão-Neto, and Glauber T Silva. Acoustic spin transfer to a subwavelength spheroidal particle. *Physical Review E*, 101(4):043102, 2020.
- [12] Hans C Ohanian. What is spin. *Am. J. Phys*, 54(6):500–505, 1986.
- [13] WA Oran, LH Berge, and HW Parker. Parametric study of an acoustic levitation system. *Review of Scientific Instruments*, 51(5):626–631, 1980.
- [14] Jung Hwan Park, Ju-Ro Lee, Sungkwon Park, Yu-Jin Kim, Jeong-Kee Yoon, Hyun Su Park, Jiyu Hyun, Yoon Ki Joung, Tae Il Lee, and Suk Ho Bhang. Subaqueous 3d stem cell spheroid levitation culture using anti-gravity bioreactor based on sound wave superposition. *Biomaterials Research*, 27(1):51, 2023.
- [15] Abhishek Saha, Saptarshi Basu, and Ranganathan Kumar. Velocity and rotation measurements in acoustically levitated droplets. *Physics Letters A*, 376(45):3185–3191, 2012.
- [16] Lu Shen, Junfei Tai, Alexandru Crivoi, Junfei Li, Steven Cummer, and Zheng Fan. Self-stabilizing three-dimensional particle manipulation via a single-transducer acoustic tweezer. *Applied Physics Letters*, 122(9), 2023.
- [17] Chengzhi Shi, Rongkuo Zhao, Yang Long, Sui Yang, Yuan Wang, Hong Chen, Jie Ren, and Xiang Zhang. Observation of acoustic spin. *National Science Review*, 6(4):707–712, 2019.
- [18] JK Richard Weber, D Scott Hampton, Dennis R Merkley, Charles A Rey, Mark M Zatarski, and Paul C Nordine. Aero-acoustic levitation: a method for containerless liquid-phase processing at high temperatures. *Review of scientific instruments*, 65(2):456–465, 1994.
- [19] WJ Xie, CD Cao, YJ Lü, ZY Hong, and B Wei. Acoustic method for levitation of small living animals. *Applied Physics Letters*, 89(21), 2006.
- [20] WJ Xie and B Wei. Dependence of acoustic levitation capabilities on geometric parameters. *Physical Review E*, 66(2):026605, 2002.

## A Acknowledgements

We were fascinated by the rotation phenomenon in water and took it as an opportunity to investigate the rotation phenomenon in the omnipresent air. The authors of this article who participated in this competition gratefully acknowledge the support of the supervising teacher, Yiming Yang, who provided us with the basic equipment to conduct the experiments and gave us access to advanced software such as COMSOL and MATLAB without asking for anything in return. Apart from him, we did not seek any other help.

The choice of topics was made by both students. We chose our topics based on our observations and reflections from our daily lives. While playing in the swimming pool, we discovered the formation of vortices in water by swirling our fingers underwater. Considering that air and water are both liquid, but the former is invisible, we ask ourselves whether there is such a swirling effect in the air. If the answer is yes, how can we make this effect visible and what property does this effect have? In water, we can see the vortex effect because of the bubbles in the middle. So in the air, we can mimic the method we used to observe the vortex underwater by positioning an object in the air and studying its behavior. The first step was obvious: to make things float in the air. We did some research and came across a technology called acoustic levitation, which allows you to keep objects, even living beings, in the air by creating the desired acoustic field. This technology has great flexibility. From one transducer to several transducers with computer skills.

After this important discovery, we bought transducers reflectors and other equipment except an oscilloscope, waveform generator, and power amplifier provided by our supervising teacher. Our supervising teacher helped us set up the equipment and we began our experiment. We used a SONY camera to take photos and pictures, and a tracker to analyze the results of our experiment and obtain experimental data. We used Original Pro to graph the data and find the R-squared value and the slope of the best-fit line of our experimental data. Student Rui Yang was responsible for taking pictures and videos, setting up the camera each time, and analyzing the tracker data. Student Ziou Yuan was responsible for setting up the other devices each time and analyzing the videos and pictures. One of the biggest difficulties in our experiment was that the tracker was difficult to level. To solve this problem, we mounted the transducer on an acrylic plate and placed a spirit level on the acrylic plate. The result was that the transducer was parallel to the floor with a deviation of no more than 1 degree (this is measured by the tracker).

As for the experimental setup, we first wanted to investigate the effect of changing the X-offset, the angle of the reflector to the horizontal, and the height on the dynamic behavior of floating small polystyrene spheres (radius: 1-1.5 mm) to familiarize ourselves with this technology, which we have never seen before (see our uploaded file for evidence). During this process, we discovered the spinning behavior of the floating spheres. We defined the goal of our experiment as investigating the phenomenon of spinning floating balls. Upon further investigation, we realized that this method of making levitated objects rotate had not been researched before, so we decided to focus on this particular method. The student Rui Yang was responsible for working out the plan for each experiment, such as the experimental target and control variables, etc. In terms of conducting the experiments, the distribution of work remained the same as in the previous section.

The simulation of Matlab and COMSOL was carried out jointly by both students. Due to the difficulty of these two powerful tools, we discussed finding a solution for our scenario. The coding part in MATLAB was one of the biggest challenges in our investigation. We used the power of artificial intelligence to help us with the coding.

Regarding the division of labor in writing the first draft, Rui Yang was responsible for writing the abstract, methodology, data analysis, mind map of discussion, and summary. Ziou Yuan was responsible for writing the introduction, discussion, and researching relevant theories and articles to our paper. After that, we exchanged our opinions on the part written by the others and improved our papers. During this process, it is difficult to reach a full agreement. To increase efficiency, we talked to our supervising teacher about our views and explanations. He gave us further insights into the opinions of each participant and finally helped us to come to a more precise and accurate conclusion with more solid explanations.

## **B MATLAB Source Code**

```
%%  
% Basic parameters %  
% Define the range of H values  
Horigin = [22.81, 21.81, 21.31, 20.81, 20.31,  
19.81], 19.31, 18.81, 18.31, 17.81, 19.31, 18.81, 18.31, 17.81
```

```

H_values = (Horigin + 5.382 + 8.4041 )

% Path to the MatlabResults folder on the desktop
results_folder = fullfile(getenv('HOME'), 'Desktop', 'MatlabResults');
if ~exist(results_folder, 'dir')
    mkdir(results_folder);
end

% Loop over each H value
for H = H_values
    % Update the H value in the simulation
    H_mm = H * 1e-3; % Convert to meters

    % Rod with concave surface calculation remains unchanged
    phi_c = 2*pi + 0/180*pi + 0*pi/6;
    theta_c = 0;
    scenter_x = 0;
    scenter_y = 0;
    scenter_z = d + Rc;

    xzsc = [cos(phi_c), -sin(phi_c); sin(phi_c), cos(phi_c)] * [scenter_x; scenter_z - d];
    xsc = xzsc(1);
    zsc = xzsc(2) + d; % Now zsc is defined
    ysc = scenter_y;
    L = -0 * 1e-3; % depth of concave: 8.4041

    Dz = H_mm - zsc; % Update Dz accordingly
    Dx = L - xsc;
    sx_n = Dx;
    sy_n = 0;
    sz_n = d + Rc + Dz;

    ver_s = [0,0,1];

    ballsurface = zeros(3, (nstep+1)*(nstep+1));
    sii = [];
    ssur = [];
    xzball1 = [];
    h = 1;
    for thetaRc = 0:2*pi/nstep:2*pi - 2*pi/nstep
        for phiRc = 0+pi/nstep : pi/nstep : pi-pi/nstep
            xball = Rc*sin(phiRc)*cos(thetaRc);
            yball = Rc*sin(phiRc)*sin(thetaRc);
            zball = d + Rc*cos(phiRc);
            ballsurface(:,h) = [xball; yball; zball];
            h = h + 1;
            ver_p = [sin(phiRc)*cos(thetaRc), sin(phiRc)*sin(thetaRc), cos(phiRc)];
            phi_sp = acos(ver_p*ver_s');
            si = Rc^2*sin(phiRc)^2*pi/nstep*pi/nstep;
            if phi_sp <= asin(R/Rc)
                ssur = [ssur, [xball; yball; zball]];
                sii = [sii, si];
            end
        end
    end

    s_length = length(ssur(1,:));
    sangle = zeros(1,s_length);
    for i = 1:s_length
        sangle(i) = acos((([0 0 Rc] * (ssur(:,i) - [0; 0; d] - [0; 0; Rc])) / Rc / Rc) - pi/2);
    end
    ends_col = find(sangle == max(sangle));

    Num = 1;
    rod_length = length(s_col) * Num;
    rod = zeros(3,rod_length);
    rodi = ones(1,rod_length) * R * d / Nstep * 2 * pi / nstep;
    for i = 1:Num
        rod(:,1 + (i-1) * length(s_col) : i * length(s_col)) = ssur(:,s_col) + i * [0; 0; d / Nstep];
    end

    srod = [ssur rod];
    Srod = 0 * srod;
    for i = 1:rod_length + s_length
        xzball1 = [cos(phi_c), -sin(phi_c); sin(phi_c), cos(phi_c)] * [srod(1,i); srod(3,i) - d];
        xball1 = xzball1(1) + Dx;
        zball1 = xzball1(2) + d + Dz;
        yball1 = srod(2,i);
        Srod(:,i) = [xball1; yball1; zball1];
    end
    sii = abs(sii);
    si = [sii rodi];
    clear sii rodi

```

```

% Digitized coordinates of SOURCE, REFLECTOR & FIELD %

Tsize = size(XT);Ssize = size(XS);

corx = [];cory = [];

for i = 1:Tsize(1)for j = 1:Tsize(2)if XT(i,j)^2 + YT(i,j)^2 <= r^2corx = [corx,
XT(i,j)];cory = [cory, YT(i,j)];endendendTcor = [corx; cory];Tcorlength = length(Tcor(1,:));

Rcor = Srod;Rcorlength = length(Rcor(1,:));

clear corx coryScor = zeros(3, Ssize(2) * Ssize(3));Scor_label = zeros(3, Ssize(2)
* Ssize(3));h = 1;for i = 1:Ssize(1)for j = 1:Ssize(2)for k = 1:Ssize(3)if YS(i,j,k) ==
0e-3Scor(1,h) = XS(i,j,k);Scor(2,h) = YS(i,j,k);Scor(3,h) = ZS(i,j,k);Scor_label(1,h)
= i;Scor_label(2,h) = j;Scor_label(3,h) = k;h = h + 1;endendendendScorlength =
length(Scor(1,:));clear i j k Xt Yt Xr Yr Xs Ys Zs

% Matrix elements %

T_tm = zeros(Scorlength, Tcorlength);T_rm = zeros(Scorlength, Rcorlength);T_rt
= zeros(Tcorlength, Rcorlength);T_tr = zeros(Rcorlength, Tcorlength);U = U0 *
ones(Tcorlength, 1);

tic;for i = 1:Scorlengthfor j = 1:Tcorlengthrij = sqrt((Scor(1,i) - Tcor(1,j))^2 +
(Scor(2,i) - Tcor(2,j))^2 + Scor(3,i)^2);T_tm(i,j) = sn * exp(-1i * 2 * pi / lambda * rij)
/ rij;endendVangle = [];for i = 1:Scorlengthfor j = 1:Rcorlengthrij = sqrt((Scor(1,i) -
Rcor(1,j))^2 + (Scor(2,i) - Rcor(2,j))^2 + (Scor(3,i) - Rcor(3,j))^2);if j <= s_lengthL1 =
sqrt((Scor(1,i) - sx_n)^2 + (Scor(2,i) - sy_n)^2 + (Scor(3,i) - sz_n)^2);if L1 < RcT_rm(i,j)
= si(1,j) * exp(-1i * 2 * pi / lambda * rij) / rij;elsevert1 = [(Scor(1,i) - Rcor(1,j));
(Scor(2,i) - Rcor(2,j)); (Scor(3,i) - Rcor(3,j))];Vert2 = Rcor(:,1:s_length) - [(Rcor(1,j));
(Rcor(2,j)); (Rcor(3,j))];for ii = 1:s_lengthVangle(ii) = acos(vert1' * Vert2(:,ii) /
sqrt(vert1' * vert1) / sqrt(Vert2(:,ii)' * Vert2(:,ii)));endVangle0 = abs(min(Vangle));if
Vangle0 < 1e-2 * piT_rm(i,j) = 0;elseT_rm(i,j) = si(1,j) * exp(-1i * 2 * pi / lambda
* rij) / rij;endendelseif j > s_lengthT_rm(i,j) = si(1,j) * exp(-1i * 2 * pi / lambda *
rij) / rij;endendend

for i = 1:Tcorlengthfor j = 1:Rcorlengthrij = sqrt((Tcor(1,i) - Rcor(1,j))^2 +
(Tcor(2,i) - Rcor(2,j))^2 + Rcor(3,j)^2);T_rt(i,j) = si(1,j) * exp(-1i * 2 * pi / lambda
* rij) / rij;endend

for i = 1:Rcorlengthfor j = 1:Tcorlengthrij = sqrt((Rcor(1,i) - Tcor(1,j))^2 +

```

$(R_{cor}(2,i) - T_{cor}(2,j))^2 + R_{cor}(3,i)^2$ );  $T_{tr}(i,j) = \text{sn} * \exp(-i * 2 * \pi / \text{lambda} * r_{ij}) / r_{ij}$ ;endendclear i%

% Pressure field %

% Set the coordinates in millimeters  
[XT, YT] = meshgrid(-r\*1e3:r\*1e3/Nstep:r\*1e3, -r\*1e3:r\*1e3/Nstep:r\*1e3);  
[XS, YS, ZS] = meshgrid(-S\*1e3:S\*1e3/nstep:S\*1e3, -S\*1e3:S\*1e3/nstep:S\*1e3, 0:S\*1e3/nstep:2\*S\*1e3);

% Adjust the Pmap indices for millimeter scale  
Pmap = zeros(Ssize(2), Ssize(3));  
for i = 1:Scorlength  
Pmap(Scor\_label(3,i), Scor\_label(2,i)) = p(i);end

% Save the Pmap data  
Pmap\_filename = fullfile(results\_folder, sprintf('Pmap\_

% Find the index of the middle line in the x-axis  
middle\_index\_x = ceil(size(Pmap, 2) / 2);

% Extract the pressure field values along the middle line in the x-axis  
middle\_line\_values = abs(Pmap(:, middle\_index\_x)) / (rho \* c \* U0 \* f);

% Plotting the pressure field values along the middle line  
figure; plot(middle\_line\_values); title(sprintf('Field Strength along the Middle Line at H = %.2f mm', H)); xlabel('Y (mm)'); ylabel('Pressure Field Strength (normalized)'); grid on;

% Manually find local minima  
minima\_indices = [];  
for i = 2:length(middle\_line\_values)  
if middle\_line\_values(i) < middle\_line\_values(i-1) & middle\_line\_values(i) < middle\_line\_values(i+1)  
minima\_indices = [minima\_indices, i];endend

% Save the local minima data  
minima\_filename = fullfile(results\_folder, sprintf('LM\_

% Plot and save the local minima points  
figure; plot(middle\_line\_values); hold on; plot(minima\_indices, middle\_line\_values(minima\_indices), 'ro', 'MarkerFaceColor', 'r'); hold off; title(sprintf('Local Minima at H = %.2f mm', H)); xlabel('Y (mm)'); ylabel('Pressure Field Strength (normalized)'); grid on;  
PlotMinima\_filename = fullfile(results\_folder, sprintf('PlotMinima\_

% Calculate gradients of the pressure field  
[gradient\_y, gradient\_z] = gradient(abs(Pmap));

% Normalize gradients  
gradient\_y\_norm = gradient\_y / max(abs(gradient\_y(:)));  
gradient\_z\_norm = gradient\_z / max(abs(gradient\_z(:)));

% Plot gradient in Y plane  
figure; imagesc(squeeze(XS(1, :, 1)), squeeze(ZS(1, 1, :)), gradient\_y\_norm); colormap jet; colorbar; title(sprintf('Gradient of Pressure Field in

```
Y Plane (H = %.2f mm)', H));xlabel('X (mm)');ylabel('Z (mm)');axis square;grid  
on;GradientY_filename = fullfile(results_folder, sprintf('GradientY_
```

```
% Plot gradient in Z planefigure;imagesc(squeeze(XS(1,:,1)), squeeze(ZS(1,1,:)),  
gradient_z_norm);colormap jet;colorbar;title(sprintf('Gradient of Pressure Field in  
Z Plane (H = %.2f mm)', H));xlabel('X (mm)');ylabel('Z (mm)');axis square;grid  
on;GradientZ_filename = fullfile(results_folder, sprintf('GradientZ_
```

```
close all;end
```